

FINAL TECHNICAL REPORT

Participation in the Mars Orbiting Laser Altimeter Experiment

NASA Grant NAG5-11575

Principal Investigator: Professor Gordon H. Pettengill
Rm 37-582d, Mass. Inst. of Technology
Cambridge, Mass. 02139-4307
Tel: (617) 253-4281

Award Period: 01/15/02 to 01/14/04

Total Amount Awarded: \$49,963.00

1. GRANT MISSION

This NASA Grant, 5-11575, has covered the active participation of the Principal Investigator, Prof. Gordon Pettengill, and his Co-Investigator, Peter Ford, in the Mars Orbiting Laser Altimeter (MOLA) Experiment, over a period of two years. This participation has included attending team meetings, developing data-reduction software algorithms, and processing data, as well as presenting several oral reports at scientific meetings. The research has concentrated on the various types of Martian clouds that were detected by the laser altimeter, with results summarized below.

2. TECHNICAL SUMMARY

The Mars Orbiting Laser Altimeter (MOLA) instrument [1,2] carried aboard the Mars Global Surveyor (MGS) spacecraft, has observed strong echoes from cloud tops at $1.064 \mu\text{m}$ on 61% of its orbital passes over the winter north pole ($235^\circ < L_s < 315^\circ$) and on 58% of the passes over the winter south pole ($45^\circ < L_s < 135^\circ$). The clouds are unlikely to be composed of water ice since the vapor pressure of H_2O is very low at the Martian nighttime polar temperatures measured by the Thermal Emission Spectrometer (TES) [3], and by an analysis of MGS radio occultations [4]. Dust clouds can also be ruled out since no correlation is seen between clouds and global dust storms. The virtually certain composition for the winter polar clouds is CO_2 ice.

Cloud Types: We have constructed a database of MOLA clouds, identified by clusters of closely grouped echoes lying significantly above the planetary surface. Each set of cloud echoes was plotted by altitude and along-track distance (see Figs. 3–5), inspected visually, and assigned to a category based on its morphology and relation to surface features. The location of clouds by latitude, sub-solar longitude (L_s), and solar incidence angle are shown in Figs. 1 and 2.

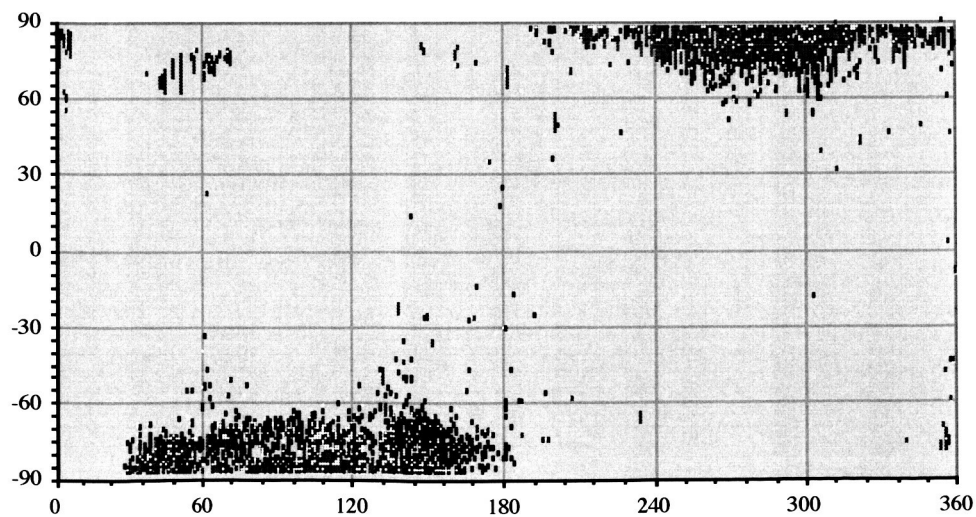


Fig. 1: Location of MOLA clouds by latitude (ordinate, in degrees) and sub-solar longitude, L_s (abscissa, in degrees).

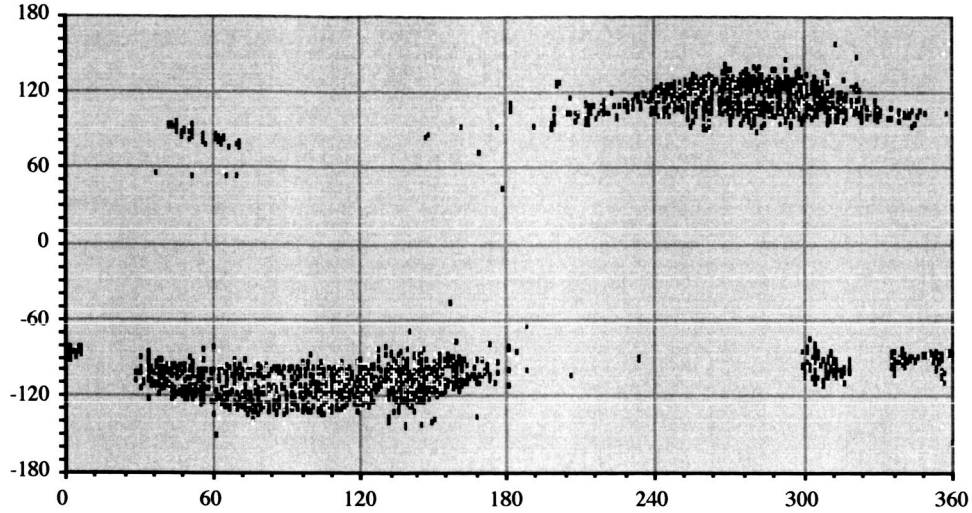


Fig. 2: Location of MOLA clouds by solar incidence angle (ordinate, in degrees) and sub-solar longitude, L_s (abscissa, in degrees). Values of solar incidence greater than $+90^\circ$ or less than -90° indicate that the sun is below the horizon. Note that virtually no clouds, except for those of the ground-hugging type (colored magenta), occur when the sun is above the horizon, as would be expected if they are composed of CO_2 ice.

The colors used to denote the cloud locations in Figs. 1 and 2 indicate the categories that we have assigned to them, as exemplified in Figs. 3–5 which show the altitude (km) and distance-along-track (km) of typical lidar echoes for the three most common categories.

Less common categories comprise *dome-shaped* clouds (colored light blue in Figs. 1 and 2), dense isolated formations not apparently associated with surface features, *ground-hugging* clouds (magenta), flat clouds that form at altitudes of less than 1 km in the spring and autumn dawn, and occasional *crater clouds* (brown), which form within large impact craters.

The data points in Figs. 3–5 have been color coded according to the time dispersion of the lidar echoes: red indicates reflection from a cloud top whose density onset varies strongly over no more than 3m of range; green and yellow denote intermediate gradients; while blue echoes are the most dispersed in range—from clouds whose density discontinuity is spread over 90m or more. Cloud echoes that saturated the MOLA receiver are colored magenta, and surface echoes are colored gray.

Under conditions of Mie scattering, and assuming unit geometric albedo, the number density of CO_2 ice particles required to produce the observed echo strengths is about $2 \times 10^8 r^{-2}$ per m^3 , where r is the particle radius in μm , which we infer to lie between $0.1\mu\text{m}$ and $50\mu\text{m}$. If r were less than $0.1\mu\text{m}$, Rayleigh scattering would predominate, the cross-section would rapidly drop off as r^{-4} , and no lidar echo would be detectable. If r were greater than $50\mu\text{m}$, the particles would fall too fast to sustain the observed wavefront patterns.

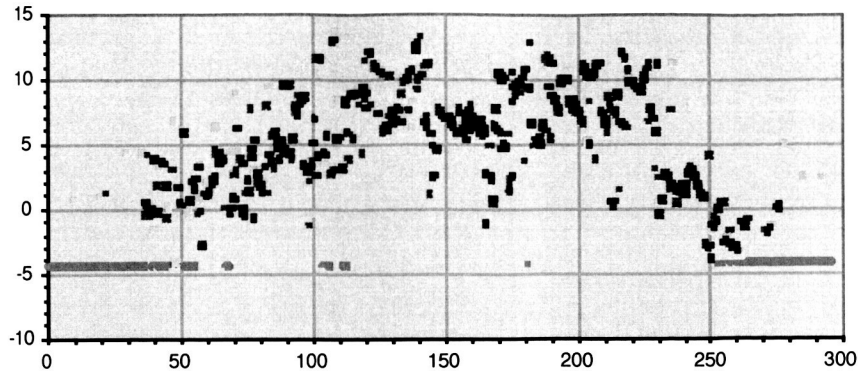


Fig. 3: Echoes from a typical cloud formation that is adjudged to contain propagating waves—green in Figs. 1 and 2—which are more common in the northern than in the southern polar regions. Ordinate represents altitude (km) and abscissa distance along track (km).

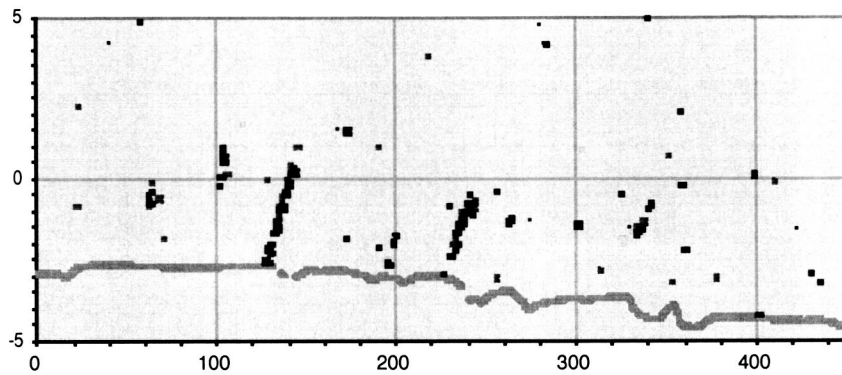


Fig. 4: Example of clouds associated with topographic features—colored blue in Figs. 1 and 2— with the appearance of mountain waves or perhaps snow tails. Ordinate represents altitude (km) and abscissa distance along track (km).

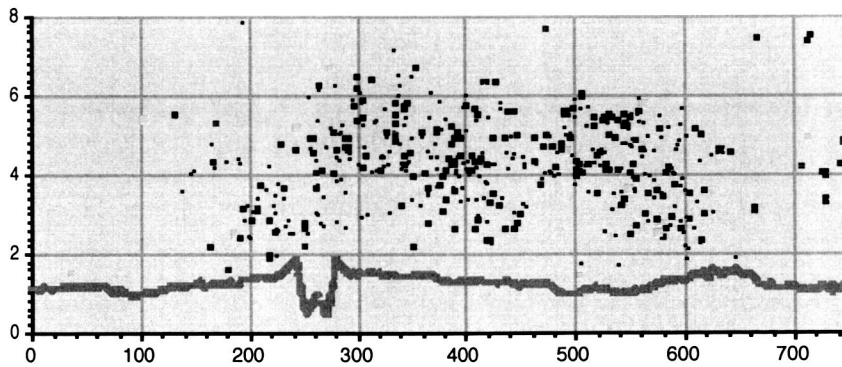


Fig. 5: Example of diffuse clouds—colored red in Figs. 1 and 2—whose lidar echoes show very little time dispersion. They are seen only in southern polar latitudes. Ordinate represents altitude (km) and abscissa distance along track (km).

Non-reflective clouds: In addition to reflective clouds, MOLA often receives no echo from either cloud or surface, thus implying an intervening absorber. These clouds form a distinct category. Their distribution in latitude, season, and solar incidence angle is shown in Figs. 6 and 7. Since these clouds are not exclusive to the polar night, and are more common during hemispheric dust storms, they may be composed largely of dust or diffuse H_2O ice, rather than CO_2 ice.

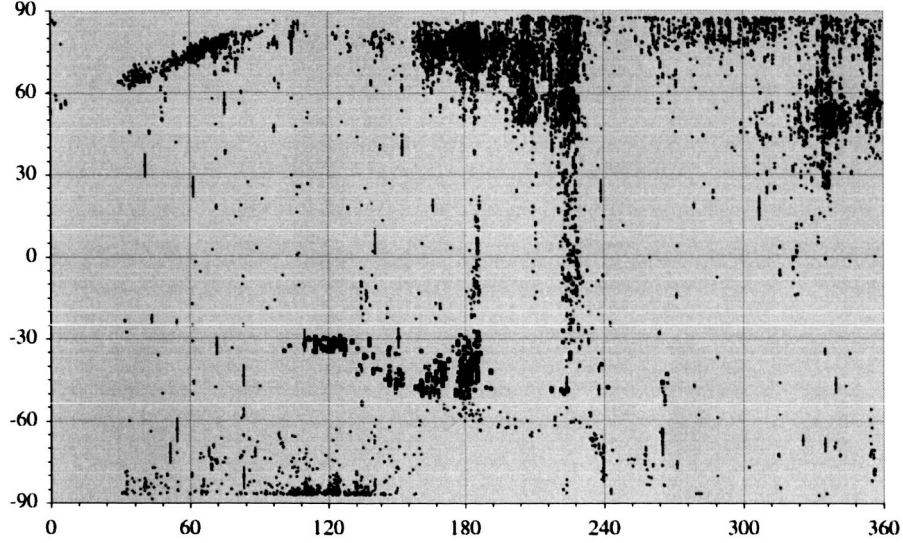


Fig. 6: Location of non-reflective MOLA clouds by latitude (ordinate) and sub-solar longitude, Ls (abscissa). Those clouds located within Hellas crater are shown in red.

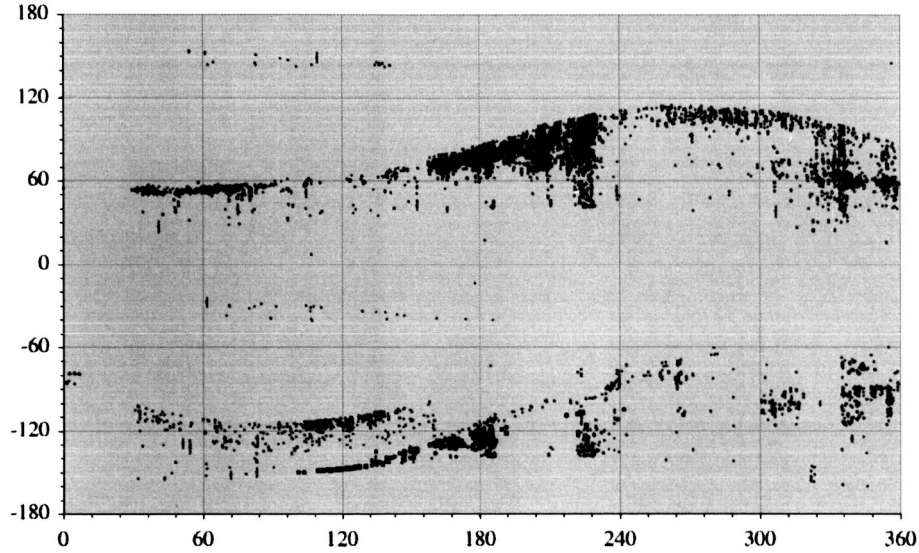


Fig. 7: Location of non-reflective MOLA clouds by solar incidence angle (ordinate) and sub-solar longitude, Ls (abscissa). Values of solar incidence greater than $+90^\circ$ or less than -90° indicate that the sun is below the horizon. Those clouds located within Hellas crater are shown in red.

Buoyancy Waves. We have identified and measured all lineaments within the cloud-top echoes, such as those visible in Figs. 3 and 4. We assume that the multiple wave fronts of the *propagating* class (Fig. 3) are buoyancy waves moving through a CO_2 atmosphere [5]. Particles of dry ice are alternately condensed and evaporated as the ambient temperature is modulated above and below the local freezing point by the passing wave. This implies that the atmosphere is close to its “wet” CO_2 adiabat at $\sim 148\text{K}$, at which point the buoyancy frequency is estimated to be $\sim 9.31 \times 10^{-3} \text{ rad/sec}$.

Spatial-Temporal Correlation. The combination of the MGS sun-synchronous orbital period, $\sim 7061 \text{ s}$, and the length of the Martian day, $\sim 88775 \text{ s}$, results in a near overlap of surface tracks at

7-day (88 orbit) intervals. However, since the tracks culminate (converge) at $\pm 86^\circ$ latitude, more frequent overlaps occur at polar latitudes. We therefore auto-correlated the locations of all clouds of a given category, assuming that they circle with the ambient wind around the pole at a nominal zonal flow. Fig. 8 shows the result of these correlations around the south pole, for a range of assumed zonal rotation rates.

Note the strong correlation at non-zero rotation rate for the class of *propagating* clouds (e.g., Fig. 3) and the relatively weak correlation between clouds related to *topographic* features (e.g., Fig. 4), suggesting that the former are moving in a polar vortex — *ca.* 5 m/sec at 75° S latitude—while the latter are not. The tracks of some correlated propagating clouds are shown in Fig. 9.

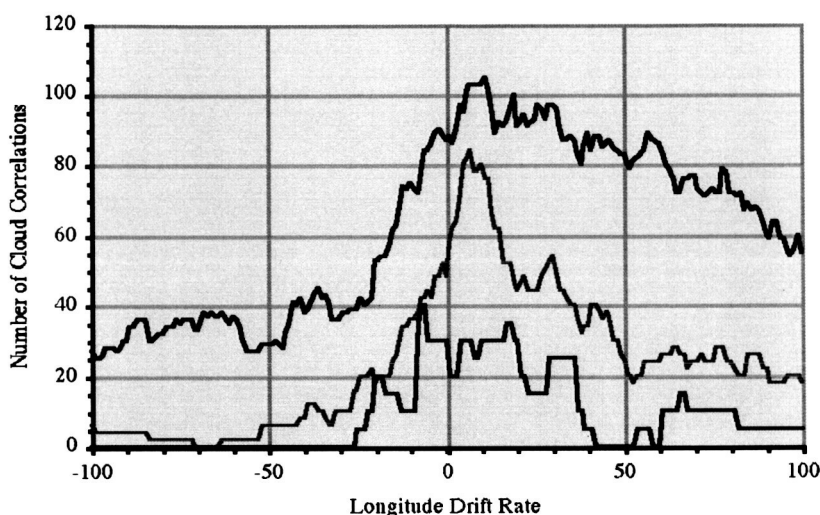


Fig. 8: Correlation between pairs of clouds detected within 48 hours of each other and separated by $> 1^\circ$ of arc measured from the center of Mars, as a function of zonal vortex wind drift rate (degrees of longitude per day). Green: correlation of propagating clouds; blue: of topographic clouds; black: of all cloud categories.

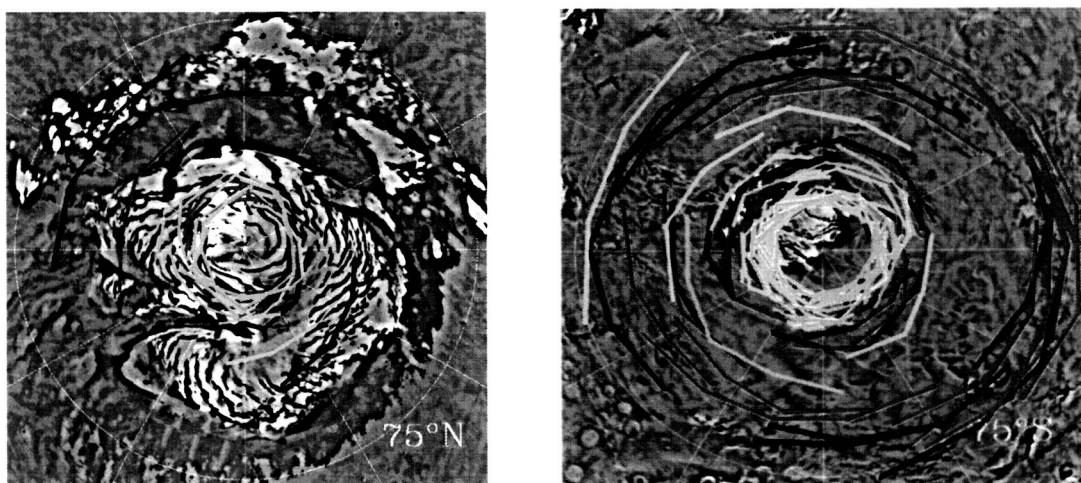


Fig. 9: Track history of correlated clouds near the North and South Poles of Mars. Color denotes the interval over which correlation was observed: pink: 1 day; green: 2 days; blue: 3 days; cyan: 4 days.

Infrared Emission. Simultaneous observations were made by MOLA and by the MGS Thermal Emission Spectrometer (TES) [6]. At the low temperatures of the polar night, the emission spectrum T_λ between $15\mu\text{m}$ and $25\mu\text{m}$ is most useful. With minimal contribution from H_2O and dust, the emission is dominated by the CO_2 rotation band at $15\mu\text{m}$ and by the thermal (Planck) spectrum from the surface and atmosphere at their respective temperatures. Although the fundamental spatial resolution of each of the 6 TES detectors is $\sim 3 \times 3$ km, all six are usually summed together for polar nighttime observations, in order to achieve detectable signal levels. Each footprint is therefore $\sim 6 \times 9$ km and encloses the ~ 200 m diameter MOLA footprint. The surface emissivity is typically ~ 0.95 at these wavelengths, so most TES observations in the polar night (see Fig. 10) show an atmosphere and surface at $\sim 148\text{K}$.

Polar “Cold Spots”: Anomalous low emission temperatures have been observed in the polar night, however, both by TES and by the IRIS instrument on Mariner 9 [7]. Fig. 10 shows TES spectra at three latitudes. On the left, at 60°S , the warm sunlit atmosphere emits strongly at $15\mu\text{m}$, but is almost transparent at other wavelengths, which are dominated by surface emission. At 85.5°S , the atmosphere is colder than the surface and absorbs at $15\mu\text{m}$, while the radiometric temperature drops at $\lambda > 20\mu\text{m}$, indicating an anomalous “cold spot.” At 79.5°S , the long-wavelength anomaly disappears and only the $15\mu\text{m}$ absorption feature remains.

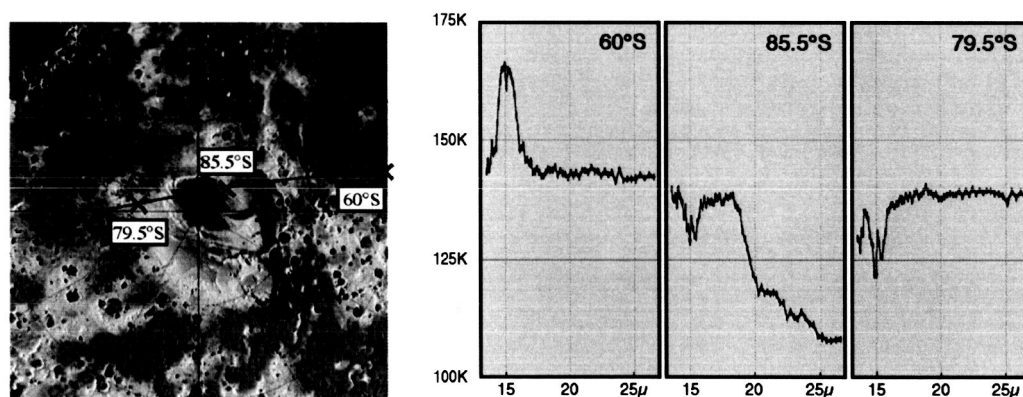


Fig. 10: Example of a cold spot. The blue line in the image on the left traces the TES track for orbit 8799, $L_s = 122^\circ$. The figure on the right shows portions of the TES spectra at three locations marked X along the orbit track. At 60°S , the upper atmosphere is warm (elevated temperatures in the $15\mu\text{m}$ CO_2 absorption band) and the spectrum beyond $18\mu\text{m}$ is consistent with 148K physical temperature and 0.95 surface emissivity. At 85.5°S , a cold spot appears, i.e., the radiative temperature falls below 140K at wavelengths longer than $18\mu\text{m}$. At 79.5°S , the anomalously low radiative temperature beyond $18\mu\text{m}$ has disappeared. The red ticks mark the wavelengths at which three contributions dominate: $15\mu\text{m}$: the atmosphere above $\sim 10\text{km}$; $17\mu\text{m}$: the atmosphere below $\sim 5\text{km}$; and $25\mu\text{m}$: the surface (physical temperature \times emissivity).

Three explanations for the cold spots have been advanced. They could result from CO_2 ice clouds [8], from a deep layer of CO_2 frost [8,9], or from surface layers of CO_2 slab ice [10]. In each case, the low value of emissivity results from volume scattering, but under very different conditions. To choose among these models, we have made maps of the spectral slope, $\partial E / \partial \lambda$, for $20\mu\text{m} < \lambda < 25\mu\text{m}$ at intervals of 5° in L_s . The cold spots show up as isolated minima, as shown in Fig. 11.

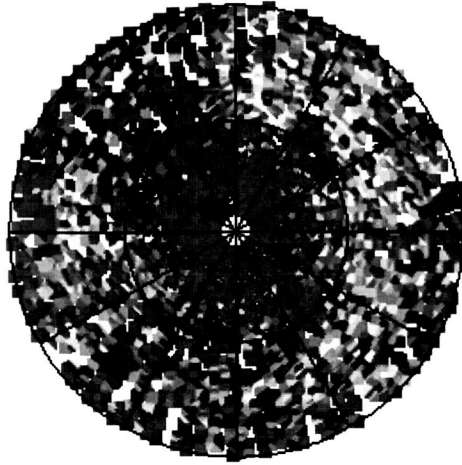


Fig. 11: Map of the TES spectral slope, $\partial T_r / \partial l$, for $20 \mu\text{m} < l < 25 \mu\text{m}$, $70^\circ < L_s < 80^\circ$ in the southern winter. Cold spots (blue, magenta) are clearly visible with negative spectral slopes

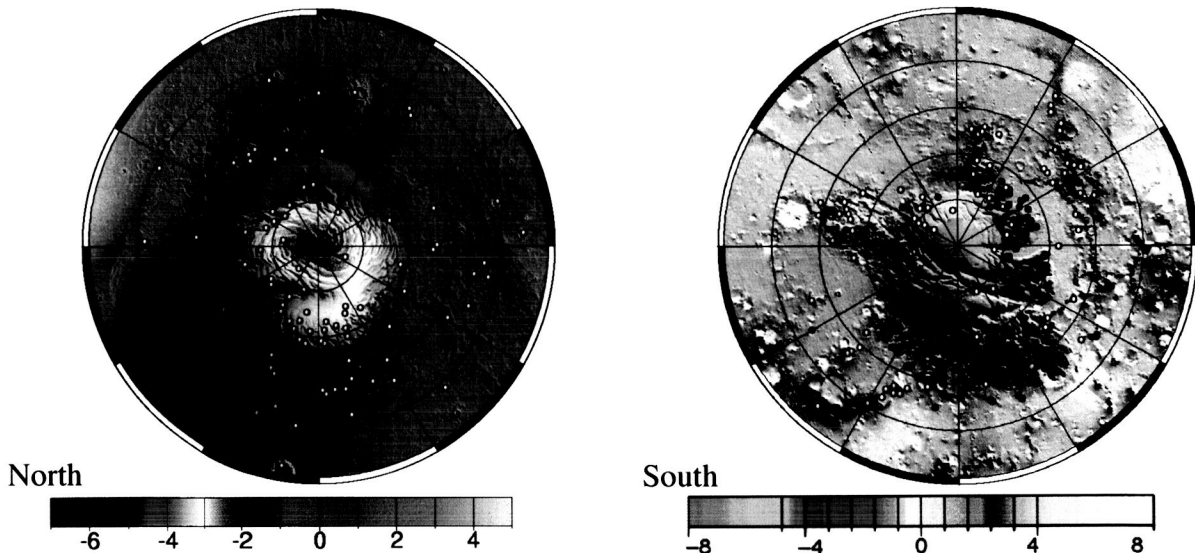


Fig. 12: The location of the 163 cold spots identified in TES observations from October 1997 to June 2001 are shown as white dots in these MOLA topographic maps. In the north, cold spots are found close to the eastern rims of 6 of the 20 largest impact craters northward of 55° latitude, and others are clustered on east-facing slopes within the permanent polar cap, but there is no significant correlation between cold spots and surface altitude. In southern polar regions, there is no significant correlation between cold spots and either altitude or surface slope or class of surface feature. As an example, the blue dots in the south polar map show the distribution of “spider” formations taken from the work of Piqueux *et al.* [11]. The spot locations also seem to be uncorrelated with several other classes of feature that are generally assumed to result from the deposition and evaporation of the seasonal cap, e.g., “dalmatian” spots, “fried egg” haloes, etc., etc. In the absence of any strong correlation with feature class, we are led to conclude that the mechanism that is responsible for the cold spots is restricted to the seasonal CO_2 layer itself.

Automatic cold spot identification: We have developed the following process for locating and measuring cold spots in TES data and correlating their occurrence with MOLA measurements:

1. Examine all TES spectra taken within 10° of nadir, and orbits for which MOLA echoes are available (3/27/98–6/29/01). Apply the Planck equation to derive radiative temperatures for

wavelengths, and estimate the average by least squares fitting. Create gridded images of the spectral derivatives, $\partial T_\lambda / \partial \lambda$, for $20\mu\text{m} < \lambda < 25\mu\text{m}$, at 5° intervals in solar longitude L_s .

2. Smooth each gridded image with a Gaussian filter of 100 km FWHM. Search for regions greater than 50 km diameter in which $\partial T_\lambda / \partial \lambda < -2.0^\circ \text{ K}/\mu\text{m}$. Confirm the identification by visual inspection and merge duplicate spots from consecutive images. Then compute the cold-spot location and diameter. This procedure results in a total of 163 cold spots, as shown in Fig. 12, 84 of them northward of 65.9°N latitude and 79 southward of 67.1°S .
3. Examine the TES archive again and determine the time at which each of the cold spots was first observed, *i.e.*, when TES footprints falling within a spot located in Step 2, smoothed by a 50 km low-pass filter, first fell below $\partial T_\lambda / \partial \lambda < -2.0^\circ \text{ K}/\mu\text{m}$.

Search for elevation change: During polar winters, the average altitude of each polar region has been observed to increase by 1–2 meters. If cold spots represent regions of recent CO_2 snowfall, it is possible that they will receive a significant fraction of their annual deposit within hours or days.

1. To investigate possible altitude changes associated with cold spots, we have collected the MOLA observations that fall within the boundary of each cold spot during a time period extending from 30 days before, to 30 days after its first appearance in TES observations.
2. Treating each cold spot independently, we begin by examining the orbits in which the MOLA footprints were reported. Pairs of orbits are selected and their points of intersection computed. Three classes of orbit pairs are distinguished:
 - a. both orbits occurred before the cold spot was first detected.
 - b. neither orbit occurred before the cold spot was first detected.
 - c. one orbit was prior to cold spot detection; the other was during or later.
3. Eliminating those crossing points that lie outside the chosen cold spot, we use the three footprints from each orbit that lie closest to the crossing point to estimate the altitude above geoid at the crossing point by quadratic interpolation. This results in two altitudes, h_i and h_j , one from each orbit. We call their difference $\delta h_{ij} = h_i - h_j$.
4. We compute the average $\langle \delta h \rangle$ and standard deviation $\sigma\{\delta h\}$ of the δh_{ij} for each of the three classes of crossing points. We also compute the standard deviation $\sigma\{\delta h_n\}$ of the δh_{ij} for each orbit n (*i.e.*, $n = i$ or j) in orbit classes “a” and “b”. In this way, we identify those orbits that systematically contribute large values to $\langle \delta h \rangle$, and whose ephemerides determined by range- and doppler-tracking are therefore suspect. After removing these orbits from the MOLA data set, we iterate the analysis procedure from Step 2 through Step 4 until no orbit contributes a $\sigma\{\delta h_n\}$ of more than 5 meters to $\langle \delta h \rangle$. This resulted in the removal of 194 from a total of 5327 orbits.

5. Cold spots possessing a wide range of topography are identified by their larger pre-cold spot values of $\langle \delta h \rangle$ and are discarded from further analysis.¹
6. Table 1 shows $\langle \delta h \rangle$, averaged over all cold spots for which the pre-spot value of $\langle \delta h \rangle$ is less than 25 cm. No significant altitude change is found to be associated with cold-spot formation
7. We repeated the analysis, Steps 1 through 5, varying the period of pre- and post-cold spot formation from 7 to 60 days, and using $\sigma\{\delta h\}$ and $\sigma\{h\}$ to filter the data as described in Step 5, above. Finally, we reran the analysis assigning random longitudes to the cold spots. In each case, no statistically significant altitude change was detected.

Table 1. Altitude variance $\langle \delta h \rangle$ averaged over all cold spots for which the pre-spot value of $\langle \delta h \rangle$ is less than 25 cm.

Number of Spots	North	South
	58	28
a. Pre/Pre (cm)	0.1 ± 3.1	-0.8 ± 7.1
b. Post/Post (cm)	3.3 ± 5.1	24.9 ± 10.2
c. Pre/Post (cm)	2.9 ± 4.1	21.2 ± 18.4

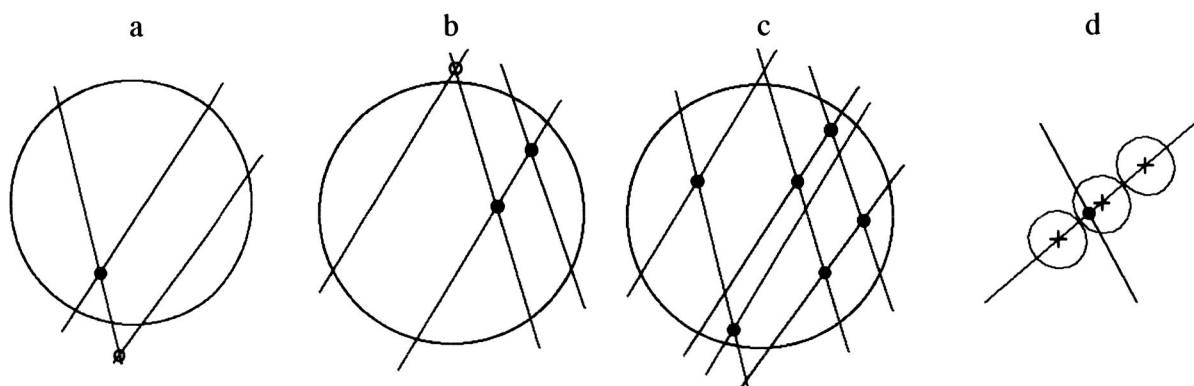


Fig. 13: Orbit Crossing Points: (a) Orbits prior to first cold spot appearance; (b) Orbits during and after cold-spot appearance; (c) One orbit before, the other after first cold-spot appearance; (d) Consecutive MOLA footprints used to interpolate the altitude at an orbit crossing-point. Orbit tracks prior to the first appearance of the cold spot are shown in red; the remainder in blue. Crossing-points that lie within the cold spot (large black circles) are shown as filled black dots; those lying outside are open black circles, and will not be included in subsequent calculations. The altitude of each valid crossing-point is estimated independently from each of the two orbits by interpolating from the nearest triplet of MOLA footprints, (see Figure d, above, in which only the post-cold spot triplet, the red circles, is shown.)

Daylight clouds: While most MOLA clouds were seen during the polar night, and were most likely composed of CO₂ ice crystals, some 3% occurred in daylight, mostly at high latitudes. In the north, these daytime clouds were restricted to three seasons: late winter ($260^\circ < L_s < 10^\circ$), mid-spring ($L_s \sim 60^\circ$), and late fall ($140^\circ < L_s < 190^\circ$). This seasonal pattern was similar to that of the

¹ We could instead have used $\sigma\{\delta h\}$ or even $\sigma\{h\}$, the standard deviation of pre-spot MOLA altitudes, as a similar measure of kilometer-scale roughness. In practice, the three metrics are highly correlated, but $\langle \delta h \rangle$ is the least sensitive to regional slopes.

non-reflective clouds (see above). In the south, daytime clouds were seen in the fall ($30^\circ < L_s < 70^\circ$) and late winter ($100^\circ < L_s < 190^\circ$), but at significantly higher latitudes than non-reflective clouds. The TES instrument measured thermal emission profiles for 58% of the MOLA daylight clouds. In no instance did the emission temperature drop below 150K in the $15\text{--}18\mu$ wavelength range, indicating that these clouds were composed of H_2O ice or dust, but not CO_2 ice.

Correlation with MOC Images: A distinctive class of daytime cloud was restricted to the late northern spring. Its MOLA echoes were closely grouped at low altitude (below 2 km, vs. 5–15 km for polar CO_2 clouds), and showed no evidence of trapped or propagating buoyancy waves. Because of the MGS sun-synchronous orbit, these clouds were observed in only two ranges of solar incidence angle: $50\text{--}55^\circ$ and $> 75^\circ$. In each instance, TES showed that these clouds lay at the boundary between an isothermal, stably stratified polar atmosphere and an adiabatic atmosphere overlying a warmer surface. Whenever they were imaged by the MOC wide-angle camera, the clouds were seen to lie at the extreme edge of the seasonal cap, as shown in Fig. 14, and were most probably composed of trapped H_2O ice and/or dust that was being released as the winter CO_2 deposits evaporated.

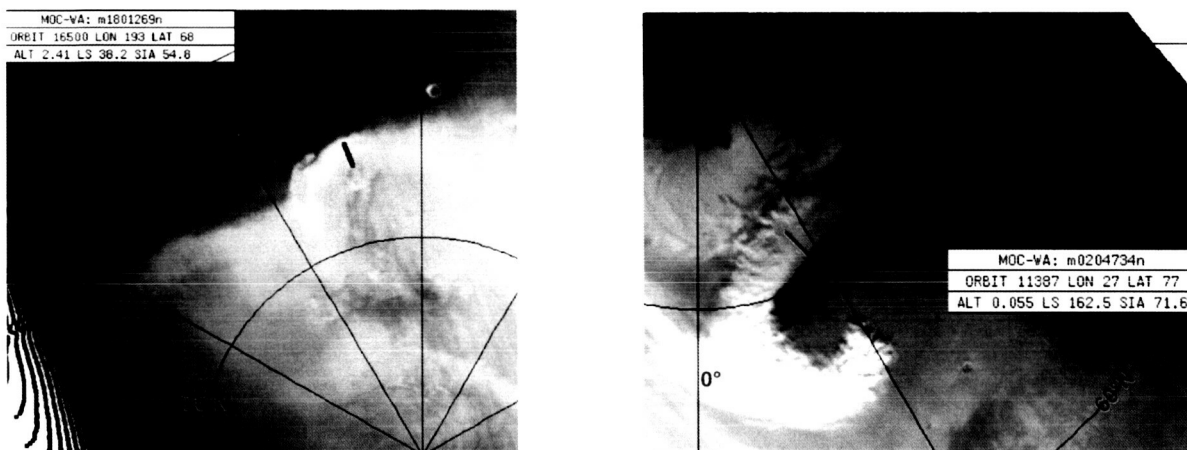


Fig. 14: Examples of daylight “surficial” MOLA clouds (green) overlaid on MOC images. In orbit 6500 (left), the cloud overlies the southern extremity of the seasonal cap, which is evaporating in the dawn sunlight. The same may be true of orbit 1387 (right), but the edge of the seasonal cap is obscured by a dust storm.

- 3.3% of MOLA reflective clouds were seen in daylight. Of these, 20% were of the rare “surficial” type
 - Of these, 55% were within MOC frames
 - Of these, 78% were located within optically dense clouds at the edge of the polar hood
- 51% of MOLA “non-reflective” clouds seen were in daylight
 - Of these, 20% were within MOC frames
 - Of these, 53% were located within optically dense clouds at the edge of the polar hood or within topographic depressions

- All clouds seen by both MOLA and MOC were observed shortly after dawn, never later.
 - In subsequent MOC frames, these clouds often became pure dust storms
 - The preference of the reflective clouds for low altitudes, and of all MOLA daytime clouds for the dawn hours, suggests that they are composed of H₂O ice condensed onto dust grains.
 - This is corroborated by the negative correlation between MOLA surficial cloud reflectivity and TES 18 μ radiative temperature

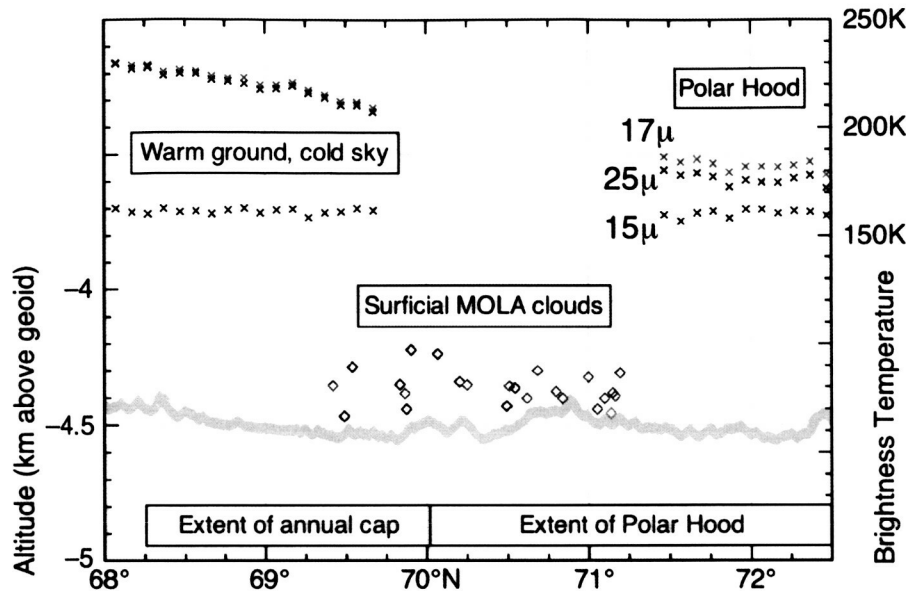


Fig. 15: TES spectra of surficial clouds observed in orbit 6883. The atmosphere at the southern (left) edge of the plot has already been warmed by sunlight for ca. 60 minutes, whereas that at the northern (right) edge is just emerging into daylight. The effect of the warming is seen in the increasing 17 μ m and 25 μ m emission temperatures, while the upper atmosphere observed in the 15 μ m CO₂ absorption band remains cold.

References

1. Zuber *et al.*, J. Geophys. Res., **97**, 7781 (1992)
2. Zuber *et al.*, Science, **282**, 2053 (1998)
3. Christensen *et al.*, J. Geophys. Res., **106**, 23823 (2001)
4. Hinson *et al.*, J. Geophys. Res., **106**, 1463 (2001)
5. Pettengill and Ford, Geophys. Res. Lett., **27**, 609 (2000)
6. Pearl *et al.*, J. Geophys. Res., **106**, 12325 (2001)
7. Hanel *et al.*, Icarus, **17**, 423 (1972)
8. Forget *et al.*, J. Geophys. Res., **100**, 21219, (1995)
9. Ditteon and Kieffer, J. Geophys. Res., **84**, 8294 (1979)
10. Titus *et al.*, EOS Trans., **80**, 611 (1999)
11. Piqueux *et al.*, J. Geophys. Res., **108**, E8, 5084 (2003)

3. MEETINGS and PUBLICATIONS

Team Meetings:

6 meetings of the Laser Altimeter Team have been held during the reporting period; of these, the PI and/or the co-I have attended 5.

Presentations:

Mars Atmosphere Modeling and Observations Workshop, Granada, Spain, January 13-15, 2003 (Ford), paper presented: "*Martian Polar Clouds.*"

Columbia Univ., Astronomy colloquium, Mar 26, 2003, (Ford); paper presented: "*Martian Polar Weather.*"

Div Plan. Sci. of the Am. Astron. Soc., Monterey, CA, September 2-4, 2003; (Pettengill & Ford); paper presented: "*Martian Daytime Clouds Observed by MOLA, TES, and MOC.*"

Am. Geophys. Un., San Francisco, December 8-12 2003; (Ford), paper presented: "*Change of Martian surface height associated with polar cold spots.*"

Other travel:

On January 28-31 2002, Peter Ford visited François Forget at the Laboratoire de Météorologie Dynamique (LMD) du CNRS, Paris to gain "hands on" experience using the LMD computers that run the Paris-Oxford general circulation model of the Martian atmosphere.

Publications.

Ford, P.G. and Pettengill, G.H., "*Martian Polar Clouds*", in preparation.

4. INVENTIONS

No patentable inventions have resulted from the research supported under this grant.

Chandra ACIS-S Spectrum of Jupiter's Aurora and Comet

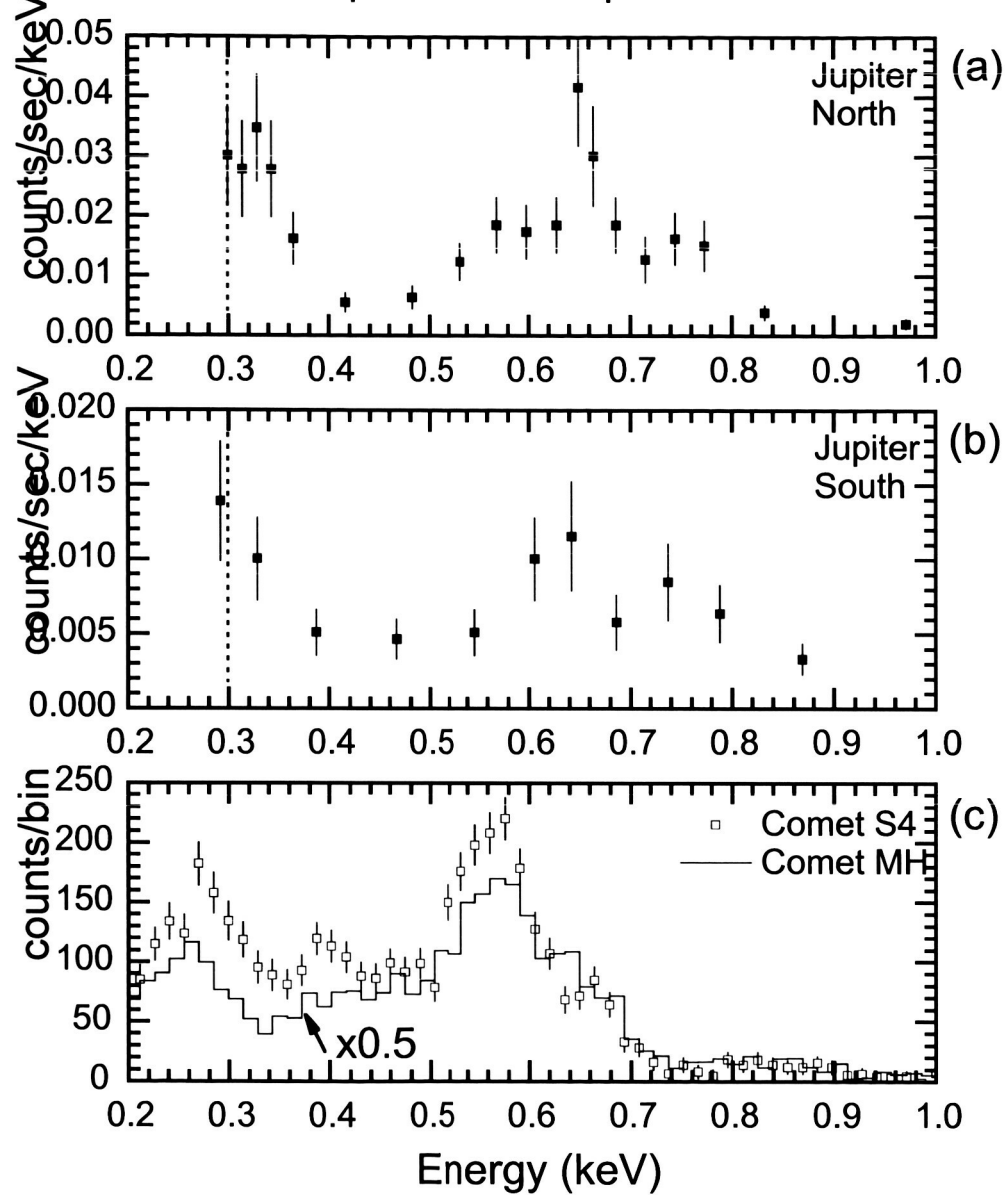


Figure 5 Jovian auroral X-ray spectrums between 300 eV and 1 keV of the north auroral region (a, upper panel) and the south auroral region (b, middle panel) as defined in figure 4. The vertical dotted line at 0.3 keV shows the low-energy cutoff for the Jovian spectra. Each spectral point represents 10 measured events which are grouped to allow further fittings. The lower global count as well as number of events of the south auroral zone compared to the north is clearly visible. Lower panel: (c) Chandra ACIS-S spectrums of comets Linear S4 [S4] and McNaught-Hartley [MH]; note that spectrum for comet MH is plotted after scaling by 0.5. Two noticeable features present in Jovian spectra but absent in comets are at around 0.65 keV and 0.75 keV.